

Investigating the effect of Na^+ , Ca^{2+} , and Cu^{2+} sorption in montmorillonite using density functional theory and molecular dynamics simulations

Yalda Pedram¹, Yaoting Zhang¹, Scott Briggs², Chang Seok Kim², Andrey G. Kalinichev³, and Laurent Karim B  land^{1*}

¹*Department of Mechanical and Materials Engineering,
Queen's University, Kingston, ON K7L 3N6, Canada*

²*Nuclear Waste Management Organization, Toronto M4T 2S3, Ontario, Canada and*

³*Laboratoire SUBATECH, UMR 6457-Institut Mines T  el  ecom Atlantique,
Nantes Universit  , CNRS/IN2P3, 44307 Nantes, France*

Montmorillonite (MMT) is the main mineral component of bentonite clay, which is currently proposed as a sealing material for deep geological repositories (DGRs) of used nuclear fuel. If copper-cladded used fuel containers corrode, Cu^{2+} ions could potentially be adsorbed by the surrounding MMT. In such a scenario, ion exchange between Na^+ and Cu^{2+} is expected. In this study, a multiscale approach that combines electronic density functional theory (DFT) and force-field-based molecular dynamics (MD) simulations was employed to study the effect of introducing Cu^{2+} ions to MMT. An extension to the ClayFF force field is parametrized and validated using DFT, to model how Cu^{2+} interact with clay systems. MD simulations were performed to calculate the interaction free energies between MMT platelets containing Cu^{2+} ions (Cu-MMT) and compared them to inter-platelet interaction energies in Na-MMT and Ca-MMT. Our calculations suggest Cu-MMT possesses swelling pressures intermediate between those of Ca-MMT and Na-MMT. Furthermore, our MD simulations suggest Cu^{2+} possesses MMT interlayer mobility similar to that of Ca^{2+} .

I. INTRODUCTION

Bentonite is used by diverse industries [1, 2] because of its high swelling potential, strong adsorption capacity, temperature durability, and low permeability [3–5]. It is added to drilling fluids within the oil and gas exploration sector [6–8], acts as an impermeable barrier for geotechnical engineering projects to prevent water infiltration [2, 9], and is used in the ceramics industry as a binding agent [2]. In the pharmaceutical and medical domains, it is utilized as a drug delivery systems, as a binder in tablet formulations and for absorbing poisons [2, 10, 11]. In environmental engineering, bentonite efficiently adsorbs heavy metals and contaminants during wastewater treatment processes [2, 12, 13].

Bentonite is also under consideration in the context of nuclear waste management, being proposed as a sealing material for deep geological repositories (DGRs) [2, 14, 15]. Proposed DGRs involve multiple barriers, typically including a radioactive waste form enclosed within a copper-coated steel container, surrounded by bentonite clay. The copper-coated canisters within this system will undergo varying environmental conditions, transitioning from an oxic environment for up to a few months to anoxic conditions thereafter [16, 17]. During the initial repository stage, oxygen atoms will interact with copper, forming a surface film of Cu_2O or CuO/Cu(OH)_2 [18]. As the oxygen is depleted, a potential risk of copper corrosion arises due to exposure to sulfide-containing groundwater [19], which could be accelerated by irradiation-induced electrolysis. Under such

a scenario, Cu ions would dissolve in the surrounding solution, likely in the form of Cu^{2+} , and would interact with the surrounding clay.

The primary component of bentonite is the montmorillonite (MMT) mineral. MMT consists of silicon tetrahedral (T) and aluminum/magnesium octahedral layers (O), forming TO and TOT layers at the nanoscale, with hydrated interlayers and hydroxyl group edges [20, 21]. A distinguishing feature of MMT is its permanent net negative charge, resulting from isomorphic metal substitution. For instance, Al^{3+} or Fe^{3+} can replace Si^{4+} in T layers, while Mg^{2+} or Li^+ can substitute Al^{3+} in O layers [21, 22]. Layer-charged MMT is balanced by hydrated cations, such as Ca^{2+} and Na^+ . The swelling mechanism of these minerals is driven by the hydration of adsorbed ions between the layers due to their high hydration energy, leading to charge neutralization; such swelling clays are also known as smectite clays [21, 23, 24].

Several experiments have shown two fundamental processes governing MMT behavior: crystalline swelling and osmotic swelling [25–27]. Crystalline swelling, linked to hydrated interlayer cations, is stepwise and confined within a 9–20   range which is observed in a wide range of clay minerals [23, 25, 28]. In contrast, osmotic swelling is a continuous process, involving a range greater than  35–40  , and results from ion concentration disparities, also increases linearly with increasing water content [23, 25]. In the osmotic swelling range, Na-montmorillonite (Na-MMT) can absorb water, expanding significantly beyond the limits of crystalline swelling [23]. Norrish *et al.* [26] reported 20-fold volume expansion of Na-MMT in both osmotic and crystalline regions. This expansion is driven by a combination of electrostatic and Van der Waals forces, as well as pressure from cations between the clay layers [25, 26]. Of note, the extent of

* laurent.beland@queensu.ca

swelling in Na-MMT is linked to multiple factors, including dry density, solution salinity, and temperature [29].

There exists a transition region known as the 'Ravina and Low' zone [30], which marks the abrupt shift between these two swelling regimes. However, this transition, referred to as *forbidden* by Ravina and Low [30], has not been observed in X-ray diffraction experiments [26, 27, 31, 32]. Fink *et al.* [27] demonstrated that this forbidden layer occurs in Wyoming Na-MMT, where isomorphic substitution occurs in both the tetrahedral and octahedral layers, and not in Na-MMTs with only octahedral substitutions. Furthermore, Meleshyn *et al.* [33] employed Monte Carlo simulations to reveal that interlayer spaces within such Na-MMTs can be locked due to a chainlike structure composed of 'substituted tetrahedron-Na cation-water molecule-Na cation-water molecule-Na cation-substituted tetrahedron' between layers. This space can remain locked until the water content approaches 850 mg/g.

Classical DLVO theory [34], named after its developers Derjaguin, Landau, Verwey, and Overbeek, describes the interactions between colloidal particles in a liquid medium. The theory considers two colloidal particles and characterizes their interaction as a balance between repulsive electrostatic forces and attractive Van der Waals forces. However, the DLVO theory fails to capture nanoscale forces between MMT platelets and the influence of divalent cations which makes it inadequate for this specific research [35–37]. Molecular dynamics (MD) simulations overcome these limitations and allow to better understand MMT at these very fine scales. Atomistic MD simulations directly probe nanoscale interactions, and are a good complement to traditional characterization methods such as scanning and transmission electron microscopy and X-ray diffraction (XRD) [38].

MMT is routinely modeled using the ClayFF force-field, developed by Randall T. Cygan and collaborators [39]. This force-field is based on electrostatic and Lennard-Jones pair interactions and will be elaborated upon in the method section. For example, Ho *et al.* [40] used a modified ClayFF force-field, as discussed later, to explore the impact of hydroxyl edges on Na-MMT hydration. Hydroxyl groups hindered the entry of the initial water layer (1-W) to the interlayer. The study indicated an alignment of the 0-W state at 9.85 Å, consistent with XRD results for dry MMT (9.6-9.8 Å) [41]. The study excluded hydrogen bonds between hydroxyl layers to assess their impact on 0-W-1-W barrier energy. Preserving hydrogen bonds led to higher barrier energy, suggesting their role as gatekeepers for water entry between interlayers. Sun *et al.* [42] used a clayFF-based model to explore swelling pressure in semi-periodic Na-MMT sheets in various solutions; swelling pressure increased exponentially with dry density, regardless of the solution, with the highest swelling pressure observed in pure water. In another MD-based study, Akinwunmi *et al.* [43] examined the swelling characteristics of periodic Ca-MMT sheets and periodic Na-MMT sheets in pure water. According to

the MD simulations, at low to moderate dry densities, Ca-MMT's swelling pressure was lesser than Na-MMT's. At high dry density, Ca-MMT exerted greater swelling pressure than Na-MMT [44].

In order to study the influence of Cu^{2+} on MMT at the atomistic level, existing ClayFF force-fields needs to be extended to handle Cu^{2+} in clay. To do so, electronic density functional theory (DFT), which is an approximation to quantum mechanics, will be employed as a benchmark to fit this extended force-field. Our main objectives are twofold. First, we parametrized and validated a novel interatomic interaction force-field for Cu^{2+} in clay, using DFT, extending the ClayFF model. Secondly, MD simulations were performed to calculate interaction energies between MMT platelets containing Cu^{2+} and Ca^{2+} counter-ions, and compared to interaction energies between MMT platelets with Na^{+} counter-ions. Additionally, the diffusion coefficients of each cation between platelets and swelling pressure of MMT platelets in the presence of Na^{+} , Ca^{2+} and Cu^{2+} are calculated.

This work is divided into the following sections: in section II we will explain the computational procedures, simulation parameters and employed MMT models. Section III is divided into three sub-sections. First, we will discuss the results of fitting procedures, then the validation of the extended ClayFF force-field and finally obtained PMFs, swelling pressures and mobility of cations will be shown.

II. METHOD

ClayFF is not designed to handle Cu^{2+} on MMT. To overcome this limitation we conducted a series of electronic density functional theory (DFT) simulations. We will begin by discussing the DFT setup. Following that, we will discuss the ClayFF force-field, which forms the basis of our simulations. The MD setup utilized to investigate the behavior of our systems will also be discussed, including an introduction to the potential of mean force (PMF) approach employed to calculate interaction free energies.

A. Density functional theory

DFT simulations were performed as implemented in the open-source software Quantum Espresso [45] with projector-augmented waves (PAW) [46–48]. The generalized gradient approximation (GGA) by Perdew–Burke–Ernzerhof (PBE) was employed to calculate the exchange-correlation energy [49]. We prepared a periodic Arizona MMT containing $2 \times 1 \times 1$ unit cells with the size of $10.54 \times 9.15 \times 6.75$ Å using the ATOM package [50] with a total charge of -2. To neutralize the negative charge of the MMT, we introduced one Cu^{2+} , resulting in Cu-MMT with the formula

$[Cu].[Si_{16}[Mg_2Al_6]O_{48}(OH)_8]$. A similar formula was used for Ca-MMT by substituting Cu^{2+} with Ca^{2+} .

The aim of studying Ca-MMT was to establish a basis for comparing it to Cu-MMT, given their shared divalent cation nature. This comparative analysis aimed to enhance the precision of MD calculations for Cu-MMT. This choice was motivated by the inclusion of Ca^{2+} within the original ClayFF package, allowing for a more accurate evaluation.

Convergence tests were performed, revealing that a kinetic energy cut-off for wave functions of 1224.5 eV (90 Ry) for Cu-MMT and 680.28 eV (50 Ry) for Ca-MMT, along with a $2 \times 2 \times 2$ Monkhorst-Pack k-point grid [51], were sufficient. Next, geometric optimization of Cu- and Ca-MMT was performed. For this purpose, seven distinct Ca-MMT and twelve Cu-MMT configurations, differing in the cation positions on the negatively charged MMT surface, were constructed. A simulation box measuring 11 Å along the Z axis was employed. Volume and ion relaxation were run for each configuration using the Broyden-Fletcher-Goldfarb-Shanno (BFGS) algorithm [52]. The total energy and force convergence thresholds were set at 1×10^{-4} eV and 1×10^{-3} atomic units of force, respectively. To determine the optimal configuration, the adsorption energy of the adsorbed ions was computed using Eq. (1):

$$E_{ads} = E_{cation-MMT} - (E_{cation} - E_{MMT}). \quad (1)$$

Here, $E_{cation-MMT}$ represents the energy of the cation-MMT system after optimization, E_{cation} denotes the energy of a single cation, and E_{MMT} signifies the energy of the optimized MMT structure.

B. Interatomic interaction potential

This subsection introduces ClayFF, which serves as the foundation for our MD simulations. Then, we detail the process of extending ClayFF for Cu^{2+} interactions.

1. ClayFF

ClayFF [24, 39] is constructed using mostly based on non-bonded interactions including Van der Waals in the form of Lennard-Jones (12-6) (L-J) function Eq. (2) and Coulombic interaction energies Eq. (3):

$$E_{VDW} = \sum_{i \neq j} 4\epsilon_{ij} \left[\left(\frac{\sigma_{ij}}{r_{ij}} \right)^{12} - \left(\frac{\sigma_{ij}}{r_{ij}} \right)^6 \right]. \quad (2)$$

$$E_{Coul} = \frac{e^2}{4\pi\epsilon_0} \sum_{i \neq j} \frac{q_i q_j}{r_{ij}}. \quad (3)$$

The parameters ϵ_{ij} and σ_{ij} denote the potential energy well depth and the distance at which the potential en-

ergy crosses 0. For simplicity, these parameters are presented for identical atoms, referred to as diagonal interaction terms. Off-diagonal terms are calculated by the Lorentz-Berthelot combination rules which use arithmetic and geometric means for σ_{ij} and ϵ_{ij} [53], respectively. ClayFF includes the flexible simple point charge (SPC) water model introduced by Berendsen *et al.* [54]. Within this model, each atom is represented by a partial charge at the center of the atom. Specifically, oxygen and hydrogen atoms within water molecules carry partial charges of -0.82 e and +0.41 e, respectively. While ClayFF maintains similar L-J parameters for all oxygen atoms as introduced in the SPC water model, the partial charges vary based on local coordination and environments. ClayFF was originally designed for infinite (periodic) clay sheets; however, several studies have modified ClayFF to investigate clay particles containing hydroxyl edges [24, 40, 55–60] by extending harmonic and Morse potential for O-H bonds, as well as harmonic potentials for the metal-O-H angles. In our present investigation, a harmonic potential is employed for the bonds and angles.

2. Training procedure for Cu^{2+} interactions

In order to train and validate a ClayFF Cu^{2+} interaction model, molecular statics and MD simulations were conducted in the large-scale atomic/molecular massively parallel simulator (LAMMPS) software package [61, 62], employing the modified ClayFF force-field [24]. For all simulations, a cut-off radius of 9.5 Å along with Ewald summation to compute long-ranged electrostatic interactions in reciprocal space were applied.

To initiate the process, we employed a periodic $2 \times 1 \times 1$ unit cell of MMT mimicking the setups utilized in DFT calculations. Within this unit cell, we considered twelve distinct Cu-MMT setups, mirroring those employed in DFT. For each of these unique Cu-MMT configurations, we performed energy minimization via a conjugate gradient algorithm [63] with at least 14 different sets of Cu^{2+} L-J parameters sourced from existing literature [64–77]. Our aim here was to identify a set of L-J parameters that best aligned with the geometric outcomes obtained from DFT.

Having identified a set of parameters that provided geometry similar to our DFT results, we proceed with validation of the extended ClayFF.

First, we evaluated the energy of each configuration in two contexts:

1. Each configuration in ClayFF in relation to the most stable structure in ClayFF.
2. Each configuration in DFT in relation to the most stable structure in DFT.

This approach was implemented for both Ca- and Cu-MMTs to ensure a comprehensive assessment of the parameterization.

Second, assessed the spatial arrangement of individual atoms within the Cu-MMT system as determined by ClayFF and compared it to that from DFT calculations. This validation procedure was applied to the Ca-MMT system. Our principal objective in this validation was to ascertain that the interatomic interactions involving Cu^{2+} within the ClayFF force-field had achieved a level of consistency on par with that attained for Ca^{2+} within the original ClayFF force-field.

Finally, since bentonite is a swelling clay, it was important to investigate the behavior of aqueous Cu^{2+} . To accomplish this, we initially created a large simulation box containing 2790 SPC water molecules with periodic boundary conditions in all dimensions. We simulated it in an isothermal-isobaric (NPT) ensemble at 300 K and 1 atm pressure. We assessed equilibration by monitoring density and the radial distribution function (RDF) of H-H, H-O, and O-O. The average density of equilibrated water during a 500 ps period was found to be $0.994 \text{ g}/\text{\AA}^3$, consistent with values from other sources [78]. Afterward, one Cu^{2+} was inserted in the middle of the simulation box, along with two Cl^- placed at the farthest distance from Cu^{2+} to minimize their interactions. The reason behind having two Cl^- was that the system had to be neutral in order to employ the Ewald summation. Water molecules within a 2 \AA radius of Cu^{2+} were removed. Subsequently, the system underwent three separate simulations, each focusing on a single set of L-J parameter. Each system was pre-equilibrated in an NPT ensemble at 300 K and 1 atm for 100 ps, then equilibrated quantities were sampled in the canonical (NVT) ensemble at 300 K using Nose-Hoover thermostat for a duration of 500 ps. Validation of the new force fields parameters involved assessing geometric characteristics of the Cu^{2+} ion and its surroundings in water, including RDF, coordination number (CN) and angular distribution function (ADF).

C. Potentials of mean force

To gain insights into the behavior of MMT in the presence of Na^+ , Ca^{2+} , and Cu^{2+} ions at the atomic scale, potentials of mean force (PMF) were computed. A PMF quantifies the variation in free energy between different states along a reaction coordinate, connecting the energies of the states of interest through a defined pathway [79–81]. In our work, PMFs are derived using force constraint technique [81], focusing on edge-to-edge and center-to-center MMT configurations. This technique involves sampling the forces acting on fixed reaction coordinates, as described by Eq. (4):

$$\Delta A_{a-b} = \int_{r_a}^{r_b} F_r dr. \quad (4)$$

Here, ΔA_{a-b} represents the difference in free energy between states 'a' and 'b', and it is computed by integrating

the force required to maintain the MMT at a specified distance of r_a and r_b .

Three different models of MMTs were built using the ATOM package [50] to calculate PMFs.

1. A small hexagonal MMT platelet which aligns with the methodology detailed in Zhang *et al.* work [28]. The prior research by Underwood and Bourg emphasized the energetic favorability of hexagonal-shaped MMTs due to their minimized number of broken silicate rings [55, 59]. This model maintains a stoichiometric ratio of 4.25:1 for Al:Mg with the charge of -8. The structural formula for the Cu-MMT is $[\text{Cu}_8] \cdot [\text{Si}_{168} \cdot [\text{Mg}_{16}\text{Al}_{68}]\text{O}_{192}(\text{OH})_{78}]$.
2. A periodic sheet of MMT with the structural formula $[\text{Cu}_{13}] \cdot [\text{Si}_{320} \cdot [\text{Mg}_{26}\text{Al}_{134}]\text{O}_{800}(\text{OH})_{160}]$.
3. A semi-periodic sheet with the structural formula $[\text{Cu}_{16}] \cdot [\text{Si}_{336} \cdot [\text{Mg}_{28}\text{Al}_{140}]\text{O}_{824}(\text{OH})_{200}]$.

In the small platelet and semi-periodic model hydroxyl groups were introduced to rectify the edges. Al-O-H and Si-O-H in the edges were integrated into the simulation via the extension of harmonic bonds and angles from the initial ClayFF force field [58].

Initially, a large box of water was structurally optimized using the conjugate gradient (CG) method. Subsequently, equilibration occurred under an NPT ensemble at a temperature of 300 K and a pressure of 1 atm. Following this, Na-MMT, Ca-MMT, and Cu-MMT were each introduced into the box of water through separate simulations. Each PMF graph was generated through a sequence of simulations, wherein the distances between two MMT platelets or sheets were incrementally increased by an average of 0.2 \AA . In each scenario, water molecules within a 2 \AA radius of each platelet were excluded to prevent overlapping water molecules with MMT platelets and to avoid undesired interactions in the initial steps of simulation. Across all simulations, 11, 12, and 14 non-edge metals located in the octahedral layers of platelets, periodic sheets, and semi-periodic sheets respectively, remained fixed. Subsequently, every system underwent pre-equilibration under NPT conditions at 300 K and 1 atm for 50 ps, followed by further equilibration and force sampling under NVT conditions at 300 K for 1 ns. A timestep of 1 fs was chosen for all simulations.

Swelling pressure calculations for Na-MMT, Ca-MMT, and Cu-MMT were determined by analyzing the gradients of PMFs at various dry densities. These dry densities, which were calculated based on the center-to-center distances between two cation-MMTs, were inspired by the approach detailed in Sun's study [42]. In addition to this analysis, we also computed the mean square displacement (MSD) for each counter-ion within the MMT clays.

III. RESULTS AND ANALYSIS

A. Cu^{2+} interatomic interactions model

1. Results of the fitting procedure

We start by presenting our DFT-calculated adsorption energies, providing an insight into the strength of interaction between cations and MMT surface. An adsorption energy of -255.73 kcal/mol for Cu^{2+} cations was obtained. The optimal position for Cu^{2+} was found just above the MMT surface, nearly in the middle of interlayer region, almost centered within the MMT ring structure. Cu^{2+} exhibited a bonding distance of 2.75 Å with Si atom and 2.08 Å and 2.06 Å with O atoms surrounding the Si atom in the tetrahedral layer of MMT. Details provided in Table I, and Fig 1 illustrates the corresponding Cu-MMT structure. An important observation here is the distinct behavior of Cu^{2+} compared to Ca^{2+} in terms of adsorption on MMT surfaces. The adsorption energy for Ca^{2+} was determined to be -147.82 kcal/mol. Interestingly, in the case of Ca^{2+} , the ion is positioned precisely in the center of a ring and in close proximity to one of the MMT surfaces, consistent with prior calculations [82].

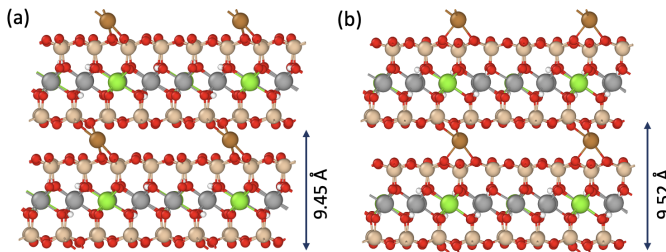


FIG. 1. Structural comparison between (a) DFT-optimized periodic Cu-MMT and (b) Cu-MMT optimized using the extended ClayFF with $\sigma = 2.21$ Å and $\epsilon = 0.05$ kcal/mol. The arrows indicate the d-spacing values. In this representation, brown, red, green, gray and beige spheres represent Cu^{2+} ions, oxygen, magnesium, aluminum, and silicon atoms, respectively.

After identifying the most stable Cu-MMT configuration using DFT, we aimed to replicate this structure with ClayFF. We performed a search involving 14 parameter sets to achieve accurate d-spacing, Cu-Si and Cu-O bonding lengths. The best-fitting L-J parameters were determined to be $\sigma = 2.13$ Å and $\epsilon = 0.05$ kcal/mol, as were proposed by K. Anitha *et al.* [66]. To further enhance the structural accuracy, we explored variations in σ , including $\sigma = 2.13$ and 2.16 Å, as detailed in Table I. $\sigma = 2.21$ Å resulted in a structure closely resembling the DFT results. Fig 1(b) illustrates the optimized Cu-MMT structure associated with the extended ClayFF. Note that Cu^{2+} as described by ClayFF resides in a different ring as compared to DFT, while maintaining similar bonding lengths and d-spacing as observed in the DFT simulations.

In addition to the parameter sets explored in this study, we evaluated a set of parameters reported by Zhang *et al.* in a recent paper [76]: $\sigma = 3.114$ Å and $\epsilon = 0.005$ kcal/mol. This L-J model closely approximated our findings, with Cu-Si bonding at 2.67 Å and Cu-O bonding at 2.14 Å and 2.09 Å, along with a d-spacing of 9.64 Å. While these parameters effectively described the Cu-MMT system in a dry environment, similar to our DFT results, our developed model exhibited higher accuracy.

We conducted a series of calculations to assess how Cu-MMT energies vary as Cu^{2+} traverses the perpendicular direction of MMT surfaces. This involved testing 40 sets of L-J parameters ranging from $\sigma = 2.11$ to 2.91 Å and $\epsilon = 0.001$ to 1 kcal/mol, in addition to the parameters employed by Zhang *et al.* [76]. The results are illustrated in Fig 2. Both sets of parameters lead to similar outcomes. Our L-J model (blue line) offers a σ value that more closely matches DFT (black line) while maintaining a comparable well depth. The softer energy curve of our model in the repulsive part will likely lead to better estimates of mechanical properties, as compared to the stiffer formulation by Zhang *et al.*

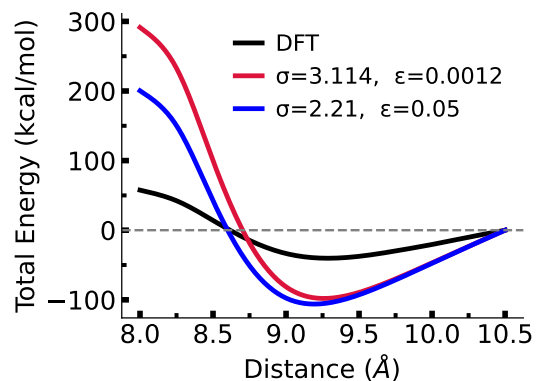


FIG. 2. A comparative analysis of the Cu-MMT energy profile along the perpendicular direction of MMT surfaces. The energy profiles are generated from DFT (black line), our best-fitted L-J parameters (blue line), and the parameters proposed by Zhang *et al.* (red line) [76].

2. Validation

First, the positions of each element in the ClayFF-optimized Cu-MMT and their counterparts in DFT simulations were compared. The deviations in the position of each element between ClayFF and DFT are visually presented in Fig 3. We also optimized Ca-MMT using both DFT and ClayFF and quantified the deviations in atomic positions from the DFT-optimized structure. The extended Cu^{2+} ClayFF model led to deviations comparable to those associated to the Ca^{2+} interaction model in ClayFF. Across all scenarios examined, the deviations

TABLE I. Structural details of optimized Cu-MMT in DFT and our best-fitted L-J parameters for Cu^{2+} in ClayFF

Method	d-spacing (Å)	Cu-Si bond (Å)	Cu-O bond (Å)
DFT	9.54	2.75	2.08, 2.06
ClayFF ($\sigma = 2.13$ and $\varepsilon = 0.05$)	9.35	2.67	2.02, 2.02
ClayFF ($\sigma = 2.16$ and $\varepsilon = 0.05$)	9.5	2.66	2.05, 2.02
ClayFF ($\sigma = 2.21$ and $\varepsilon = 0.05$)	9.5	2.68	2.06, 2.05

were consistently less than 0.26 Å.

Another analysis involved comparing the Ca^{2+} and Cu^{2+} adsorption energies for each configuration relative to the minimum energy state using either ClayFF or DFT. As illustrated in Fig 4, the extended ClayFF successfully described the lowest-energy Cu^{2+} site, and a DFT and ClayFF energies are correlated. The DFT-ClayFF correlation pertaining to Cu-MMT is more robust than that pertaining to Ca-MMT. According to DFT, the magnitude of the adsorption energies in Cu-MMT are larger than those involved in Ca-MMT. ClayFF captures this effect, albeit exagerately so. DFT suggests Cu^{2+} adsorption energies range between 0 and 17 kcal/mol—relative to the lowest-energy site—ClayFF suggest a 0 to 35 kcal/mol range, as compared to 0 to 8 kcal/mol for Ca-MMT. As we show in the further sections, this disparity does not seem to have a material impact on inter-platelet interaction forces, nor inter-platelet diffusion coefficients.

Validation of the extended ClayFF model in a hydrated environment involved assessing the geometric properties of Cu^{2+} ions immersed in water, including RDF, CN and ADF. We considered the three best-performing sets of L-J parameters found as detailed in Table II. Fig 5 highlights the results achieved using the optimal parameters, $\sigma = 2.21$ Å and $\varepsilon = 0.05$ kcal/mol. In Fig 5, the RDF for $\text{Cu-O}_{\text{Water}}$ is depicted by the blue line, while the hydration number of Cu^{2+} is shown in red. The first peak in the RDF corresponds to the average distance between Cu^{2+} and the oxygen atoms in its first hydration shell, measuring 2.04 Å. A visual representation of Cu^{2+} 's first hydration shell is provided in Fig 5. The second peak in the RDF, located at 4.24 Å, signifies the distance between Cu^{2+} and the oxygens in the second hydration shell. Coordination numbers were determined by integrating the $\text{Cu-O}_{\text{Water}}$ RDF. The analysis of the first coordination number, representing the count of oxygen atoms in the first hydration shell, confirms that the new force fields favor a 6-fold coordination for Cu^{2+} cations in the water solution, consistent with previous studies, as elaborated in Table II [83–87]. The second-shell coordination number, calculated for distances between 3 Å and 4.8 Å, was found to be 12.3, closely aligning with results from quantum mechanical/molecular mechanical molecular dynamics (QM/MM MD) simulations [85], which are also compared in Table II. Additionally, the ADF of O-Cu-O for the first hydration shell around the Cu^{2+} ion, as presented in Fig 5, indicated angles of 89.5° and 175.5°. These results demonstrate excellent agreement with find-

ings from other studies [85–90]. However, note that certain quantum effects observed using QM approaches, such as Jahn-Teller inversion, cannot be replicated using classical force-fields.

B. Potentials of mean force

We conducted a series of MD simulations using the extended ClayFF force field to calculate potentials of mean force (PMF) profiles in wet MMT systems. Our study includes four different scenarios, including both center-to-center and edge-to-edge configurations of MMT platelets. The rationale behind exploring various systems lies in the recognition that MMT platelets in real-world settings exhibit a wide range of sizes, shapes, and spatial arrangements when interacting with each other.

1. Measured potentials of mean force

Our investigation was initiated by examining the behavior of two center-to-center MMT platelets, including Na^+ , Ca^{2+} , and Cu^{2+} , in separate simulations. The resulting average PMF curves, along with a snapshot illustrating the Na-MMT structure at a specific center-to-center separation, are presented in Fig 6. Remarkably, the PMF curves, irrespective of the cation type, reveal a rich landscape of local energy minima, corresponding to various hydration states. These states encompass configurations with zero water layers (0-W), one water layer (1-W), and two water layers (2-W) inserted between the MMT platelets. Notably, the transitions between the 0-W and 1-W states, as well as between the 1-W and 2-W states, consistently occur at distances of approximately 2.5-3 Å. This distance closely matches the diameter of a water molecule and aligns with experimental measurements of hydration forces observed between diverse surfaces, including mica and MMT materials [35, 36, 93, 94]. There is a pronounced repulsive interaction at distances less than 16 Å. There are substantial energy barriers situated at 10.5-11.5 Å for the hydration process from the 0-W to 1-W state. These energy barriers can be partly attributed to the contribution of hydrogen bonding at the edges of the platelets. This observation is consistent with a prior study [40], which demonstrated that hydrogen bonds at the platelet edges serve as gatekeepers, controlling the entry of water molecules into the interlayer spaces of MMT. This effect primarily influences

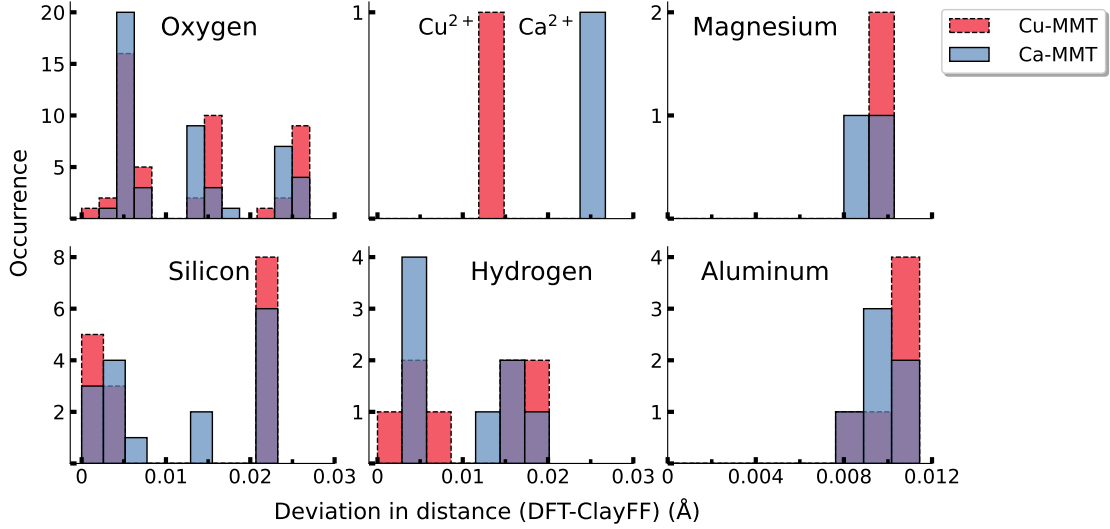


FIG. 3. Deviation between particle positions as predicted by ClayFF and DFT after structural relaxation. Ca- and Cu-MMT are shown in blue and red, respectively.

TABLE II. Comparison of Cu^{2+} hydration shell properties obtained using various methodologies, including Cu- O_{Water} length and coordination number (CN) for the first and second hydration shells, along with the O-Cu-O angle in the first hydration shell.

Method	Cu-O _{1st} hydration shell (Å)	CN _{1st}	Cu-O _{2nd} hydration shell (Å)	CN _{2nd}	Angle _{O-Cu-O} (degree)
ClayFF ($\sigma = 2.13$ and $\varepsilon = 0.05$)	2.02	6	4.28	12.8	88.5, 175.5
ClayFF ($\sigma = 2.16$ and $\varepsilon = 0.05$)	2.02	6	4.27	12.64	88.5, 174.5
ClayFF ($\sigma = 2.21$ and $\varepsilon = 0.05$)	2.04	6	4.24	12.3	89.5, 175.5
HF/MM+3bd MD [83]	2.08	6	4.2	14.5	
EXAFS/LAXS [84]	1.95, 2.29	6	4.17	8	
B3LYP QM/MM [85]	2.02, 2.29	6	4.13	11.9	89, 173
CPMD [91]	1.96, 1.96	5			
CPMD [88]	2, 2.45	5	4.03	8	90, 180
ReaxFF [86]	1.94, 2.27	6	4.27	12.5	90, 176
Neutron diffraction [87, 92]	1.97	6			
X-ray diffraction [87, 89]	1.98, 2.39	6	3.96	11.1	
X-ray diffraction [87, 89]	1.98, 2.34	6	3.95	11.6	
X-ray diffraction [87, 90]	2.01, 2.33	6	4.2	7.6	

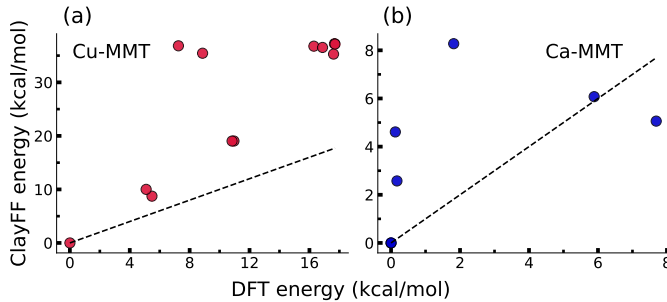


FIG. 4. Adsorption energy-setting the lowest-energy site at zero-comparison. ClayFF and DFT calculations describing (a) Cu^{2+} and (b) Ca^{2+} adsorbed on different MMT surface sites after structural relaxation are compared. Dashed lines represent a one-to-one relationship.

the first layer of hydration. The initiation of the swelling process is found to depend on breaking hydrogen bonds and was influenced by the size and shape of the MMT platelets [40]. The differences between the two local energy minima indicate the relative stability of different hydrated states. The significant difference between minima at 0-W and 1-W for all structures underscores the strong preference of MMT platelets for water absorption. Furthermore, the energy difference between 0-W and 1-W of Na-MMT is lower than that observed for Ca- and Cu-MMT, possibly due to variations in the hydration energy of the first water shell around different cations. Additionally, the larger size of hydrated Cu^{2+} leads to its local energy minima being located at a slightly greater distance as compared to the other two cations.

In our study, we conducted PMF calculations for in-

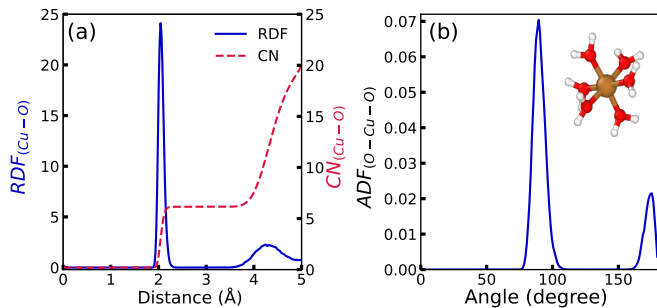


FIG. 5. (a) Radial distribution function (RDF) of $\text{Cu-O}_{\text{Water}}$ for hydrated Cu^{2+} in the flexible SPC water model. The solid blue line represents the RDF and the dashed red line represents the coordination numbers (CN). (b) Angular distribution function (ADF) of $\text{O}_{\text{Water}}\text{-Cu-O}_{\text{Water}}$ in the first hydration shell.

interactions involving two edge-to-edge platelets according to Fig 6. This type of interaction does not exhibit significant dependence on the cations present in the environment. While the local minima in edge-to-edge interactions are not as pronounced as those observed in center-to-center interactions, we observe an oscillation pattern in the PMF profiles. This pattern is attributed to the presence of water layers positioned between the two platelets.

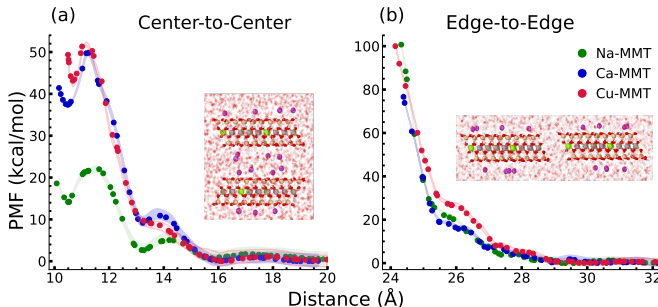


FIG. 6. Potentials of mean force (PMF) for (a) center-to-center interactions of Na-, Ca-, and Cu-MMT platelets, and (b) edge-to-edge interactions of the aforementioned structures. The PMF results, represented by dots, are averaged, and the shaded colors indicate the variability obtained from 100 bootstrap samples.

Another assessment involved studying the interaction between a single small platelet and an infinite (periodic) sheet to replicate the interaction between small and significantly larger platelets. The resulting PMF and an illustration of the system are presented in Fig 7. The average PMF curves share similarities with those of individual platelets. However, the initial energy barrier for the transition from 0-W to 1-W is lower compared to that observed for small platelets. This discrepancy can be attributed to the reduced contribution of hydrogen bonds in these interactions. The interaction energies exhibit oscillatory patterns as a consequence of the hydration

forces that come into play when increasing the size of a single MMT layer, while also decreasing the influence of hydrogen bonds.

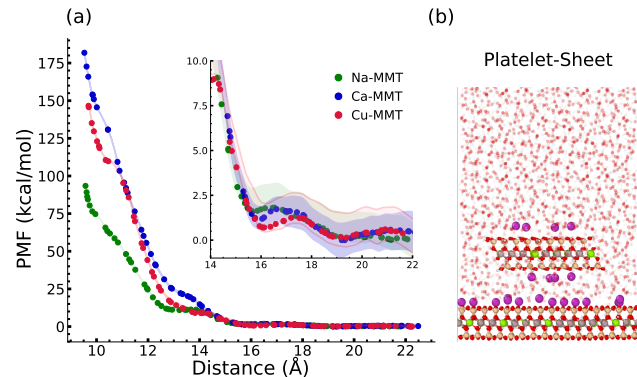


FIG. 7. Potentials of mean force (PMF) for center-to-center configuration between one periodic sheet and one small platelet of Na-, Ca- and Cu-MMT. (a) The PMFs, represented by dots, are averaged, and the shaded colors indicate the variability obtained from 100 bootstrap samples. The zoomed-in graph reveals a well-defined third water minimum. (b) Corresponding structure for Na-MMT is shown.

The latest set of calculated PMF profiles, as depicted in Fig 8, pertains to the interaction between two semi-infinite (semi-periodic) sheets of MMT. This system effectively mimics the behavior of very large platelets while considering the influence of hydrogen bonds at the edges of these sheets, providing valuable insights into the interaction dynamics at this larger scale. As illustrated in Fig 8, the overall shape of the PMF curves exhibits similarities with those observed for smaller platelets. One important feature, as revealed by the zoomed-in PMF graphs in Fig 8, is the distinct behavior regarding water adsorption when the d-spacing exceeds approximately ~ 21 Å. In this specific region, Na-MMT continuously adsorbs water without encountering any significant energy barriers. It appears to transition beyond the crystalline region, a phenomenon that aligns with a previous study on Arizona Na-MMT, which demonstrated the absence of forbidden layers in its structure [27]. In contrast, Ca-MMT and Cu-MMT face relatively minor energy barriers in this d-spacing range and do not exhibit swelling. This disparity in behavior could be attributed to the presence of forbidden layers, as observed in the work of Meleshyn *et al.* for Wyoming Na-MMT [33]. The concept of forbidden layers arises from the chainlike structure formed by Na^+ ions and water molecules in the interlayer region. In the case of Wyoming Na-MMT, Na^+ ions form an inner complex, however; in Arizona MMT substitution occurs in the octahedral layer and Na^+ forms outer-sphere complex. This leads to the absence of forbidden layers in Arizona Na-MMT. However, it is plausible that Ca^{2+} and Cu^{2+} ions, due to their higher charges, form inner complexes with the Arizona MMT layers, resulting in the creation of forbidden layers. An experimental study us-

ing low-angle XRD has demonstrated that Ca-Wyoming, Ca-Otay bentonites, and Ca-hectorite undergo a stepwise expansion, ultimately expansion stops at d-spacing of 19.6 Å for Ca-Wyoming and 22 Å for other two clays [27]. These findings support the presence of forbidden layers in Ca-MMT.

2. Swelling pressure

We employed the slopes derived from average PMFs to interpolate swelling pressures of Na-, Ca- and Cu-MMT. Additionally, we determined distances to establish dry densities, relying on the methodology introduced by Linlin Sun *et al.* [42], which involved the conversion of d-spacing data into dry densities.

Our primary objective in conducting these calculations was to quantify and compare the swelling pressures induced by Cu-MMT systems with those of Na-MMT and Ca-MMT. To the best of our knowledge, limited information is available regarding the swelling pressures of Cu-MMT.

The obtained swelling pressures from our simulations are visually presented in Fig 9, marked with filled diamond symbols. An exponential trend emerges as we examine the relationship between swelling pressure and dry densities, consistent with patterns observed in previous experimental and simulation studies with pure water and saline solutions [42, 43, 95, 96]. To validate our simulation results, we compared them with data from experimental studies. In Fig 9, we include swelling pressure for 24 different bentonites, each with different compositions or exchangeable cations (Clay materials (Exp.1)) [97]. We also reference the swelling pressure data for Wyoming MX-80 bentonite, dominated by either Ca (Ca-MMT (Exp.2)) or Na (Na-MMT (Exp.2)) [98]. Additionally, we present measurements of swelling pressure in bentonite (Exp.3) containing 50-60% MMT with Ca^{2+} and Mg^{2+} exchangeable cations [96], and compared them with Bucher *et al.* and Sitz *et al.* work (Bentonite (Exp.4-5)) [99, 100].

At lower densities, below 1.5 g/cm³, our results are consistent with experimental data which are shown by empty circled markers [96–100], revealing relatively high pressures for Na-MMT as compared to Ca- and Cu-MMT. However, as we venture into higher-density regimes, the swelling of Ca-MMT surpasses that of Na- and Cu-MMT, with Cu-MMT occupying an intermediary position between the other two. In this higher-density region, our calculations exhibit a tendency to overestimate swelling pressures as compared to available experimental results. This disparity can be attributed to the fact that our simulated models involve two perfectly stacked MMT clays, whereas natural bentonite clay typically comprises mineral impurities, including both non-oriented swelling and non-swelling minerals. Also, water percentage used in experiments and simulations can affect the results (in other words, the reference experiments are highly sensi-

tive to environmental conditions).

The swelling pressure induced by Cu-MMT lies between that of Ca-MMT and Na-MMT. The higher swelling pressure exhibited by Ca-MMT at high densities can be attributed to its elevated coordination numbers, typically in the range of 7.6 to 8.1, with Ca^{2+} -O distances of approximately 2.44-2.49 Å from its first hydration shell [101–103]. In contrast, Na^{+} ions exhibit coordination numbers of 4.9-5 with Na^{+} -O distances of about 2.4 Å [104]. These comparisons suggest that Cu^{2+} , with a coordination number of 6, should indeed generate a swelling pressure between that of Ca- and Na-MMT, particularly at high dry densities.

C. Mobility of interlayer cations

The PMF calculations for the semi-periodic MMTs identified approximate local minima for each structure, allowing us to track the trajectories of interlayer ions and subsequently compute their mean square displacements (MSD). In this analysis, we considered only those ions that remained within the interlayer region throughout the entire simulation.

The MSD graphs presented in Fig 10 depict the mobility of ions for three different water content scenarios: 1-W, 2-W, and 3-W layers. Across all scenarios and in all directions, Na^{+} ions exhibited higher mobility than the other ions. While the MSD graphs display fluctuations, we quantified ion self-diffusion coefficients (D) and reported them with uncertainties in the form of standard errors, as detailed in Table III.

The obtained diffusion coefficients revealed that, although with an increase in the number of hydrated layers, the diffusion in the Z-direction (perpendicular to the surface of MMTs) slightly increased for all ions, it remained negligible across all cases. Therefore, we considered the total diffusion in the XY plane.

The self-diffusion coefficients of Na^{+} ions in the 1-, 2-, and 3-W scenarios are consistent with prior literature, aligning closely with values of 0.53-1.09, 3.6-6.5 and $5.3-7.9 \times 10^{-10} \text{ m}^2/\text{s}$ reported at temperatures of 298 K and 323 K [105].

Similarly, the self-diffusion for Ca^{2+} ions closely match findings from previous MD simulations involving highly charged MMT structures of -0.75 e per unit cell [106]. This study reported self-diffusion coefficients of 0.6, 1.2, and $2.2 \times 10^{-10} \text{ m}^2/\text{s}$ for 1-, 2-, and 3-W states, respectively, which is relatively consistent with our observations for MMT containing 0.67 e per unit cell.

Ca^{2+} ions displayed lower diffusion compared to Na^{+} ions, a consistent trend attributed to the more stable coordination shell of Ca^{2+} as reported in prior research [31]. Our simulations also highlighted the greater escape of Na^{+} ions from the interlayer region in comparison to Ca^{2+} and Cu^{2+} ions.

Interestingly, the diffusion pattern of Cu^{2+} ions closely resembled that of Ca^{2+} ions across all directions and for

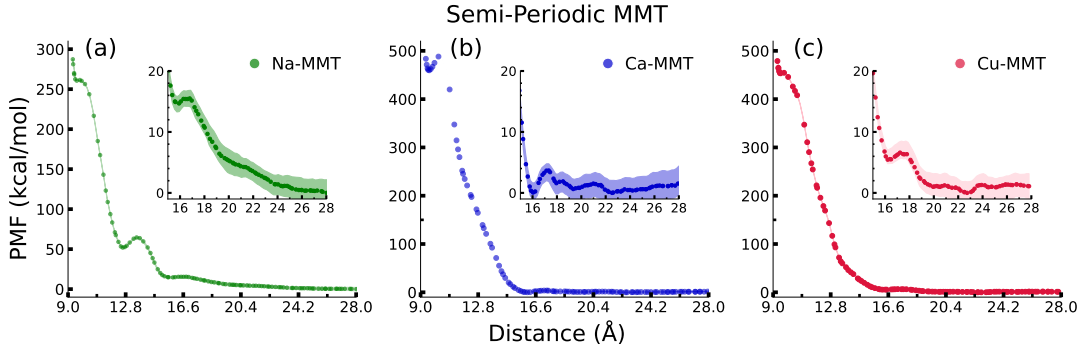


FIG. 8. Potentials of mean force (PMF) for center-to-center orientation of two semi-periodic (a) Na-, (b) Ca- and (c) Cu-MMT. The PMF results, represented by dots, are averaged, and the shaded colors indicate the variability obtained from 100 bootstrap samples. Interestingly, the zoomed-in graph shows a higher slope for the Na-MMT interaction compared to Ca and Cu-MMT.

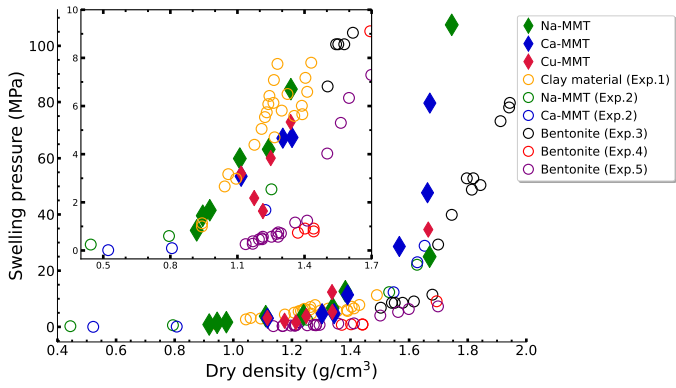


FIG. 9. Comparison of simulated swelling pressures of Na-, Ca-, and Cu-MMT with experimental results as a function of dry density [96–100].

all three hydration layers. This indicates that Cu^{2+} ions share certain mobility characteristics with Ca^{2+} ions in this context.

We noted higher diffusion rates in the second layer of water than in the third layer. This observation contrasts with some prior studies [31, 105]. We attribute this difference to our use of semi-periodic clay in simulations. The structural edges in our setup hinder the exclusion of ions from the second layer of water, subjecting them to stronger repulsive forces due to their charges and ultimately increasing their mobility. This effect is less pronounced in the third layer of water due to the reduced influence of the structural edges. In other words, our system exhibits an inherent asymmetry. It is periodic in the Y-direction while infinite in the X-direction. This asymmetry contributes to the observed differences in diffusion between the X- and Y-directions.

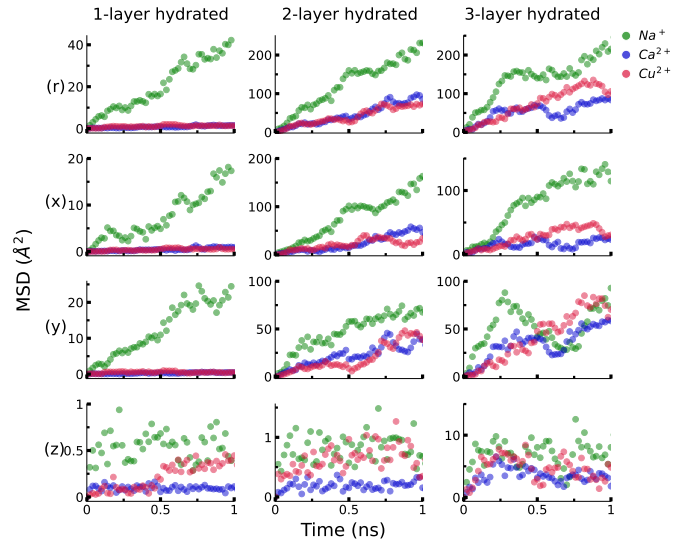


FIG. 10. Mean square displacement (MSD) calculations for interlayer Na^+ , Ca^{2+} , and Cu^{2+} ions in one, two, and three hydrated layers. Columns represent the number of hydrated layers: first column (1 layer), second column (2 layers), and third column (3 layers). Rows display total MSD, as well as x, y, and z components of the MSD.

IV. DISCUSSIONS AND CONCLUSIONS

In this work, we employed DFT calculations for Cu-MMT and extended the ClayFF force field to include Cu^{2+} interactions, allowing for the accurate modeling of Cu-MMT systems. We examined the interaction energies between two MMT with three different cations including Na^+ , Ca^{2+} , and Cu^{2+} . Our calculations suggest that, in pure water solution, the swelling pressure induced by Cu-MMT falls between that of Ca-MMT and Na-MMT, a significant observation with implications for DGR applications. Our study suggests that exerted swelling pressure caused by Cu-MMT on the container is comparable to those of Ca- and Na-MMT. Also, Cu-MMT exhibits

TABLE III. Comparison of self-diffusion coefficients (in 10^{-10} m²/s) for Cu²⁺, Ca²⁺, and Na⁺ at three different hydration levels in the interlayer regions.

Layers of hydration	D _{Na+}	D _{Ca²⁺}	D _{Cu²⁺}
1-layer hydrated			
X-direction	0.83 ± 0.04	0.05	0.03
Y-direction	1.23 ± 0.05	0.02	0.01 ± 0.01
Z-direction	0	0	0.02
Total	1.03 ± 0.03	0.04	0.03
2-layer hydrated			
X-direction	7.86 ± 0.2	2.39 ± 0.13	1.42 ± 0.12
Y-direction	2.85 ± 0.14	1.76 ± 0.11	2.13 ± 0.12
Z-direction	0.01	0	0.02
Total	5.36 ± 0.13	2.08 ± 0.08	1.78 ± 0.06
3-layer hydrated			
X-direction	5.8 ± 0.32	1.09 ± 0.13	1.81 ± 0.15
Y-direction	2.18 ± 0.42	2.88 ± 0.2	3.64 ± 0.2
Z-direction	0.09 ± 0.04	0.02 ± 0.02	-0.01 ± 0.04
Total	4.04 ± 0.24	1.99 ± 0.16	2.72 ± 0.15

substantial swelling capabilities similar to Na- and Ca-MMT, effectively hindering bacterial activities, which is crucial for the containment of radioactive waste. Of note, in a DGR system, the actual conditions might involve the presence of saline solutions, which could influence the Cu ion charge state, the swelling pressure induced by Cu-MMT and its implications for DGR applications.

Furthermore, our MSD studies demonstrated that Na⁺ ions exhibit higher mobility than Ca²⁺ and Cu²⁺ ions, particularly in the XY plane. We observed higher diffusion rates for ions in the second layer of water compared to the third layer, a phenomenon which could be attributed to the presence of structural edges in our semi-periodic clay setup.

As expected, we found similarity between the mobility patterns of Cu²⁺ and Ca²⁺ ions in our simulations. Both

ions exhibited comparable diffusion rates in all directions and for all three hydration layers. This observation suggests a common behavior in their interactions with the clay matrix, despite their different chemical properties.

In this research, we considered Cu²⁺ as the charge state of copper ions in the clay systems. However, copper may exist in other charge states. This assumption is empowered by the results of energy profile analysis of more than 40 L-J potentials for Cu²⁺ along the perpendicular direction of MMT, which two of the best results are presented in Fig 2. Surprisingly, even with a variety of potentials, we could not find a well-matched energy profile with DFT results. This discrepancy suggests that the charge of the copper ion may not be exactly 2+ in the presence of dry MMT. Furthermore, it is possible that the charge of the copper ion varies with its distance from MMT. In future, we will explore the charge distribution of copper ion using Bader charge analysis in dry and wet clay systems to gain deeper insight into this phenomena.

Overall, our findings provide a better understanding of the behavior of interlayer cations in clay systems. The extension of the ClayFF force field to include Cu²⁺ interactions enhances its versatility and applicability in modeling a broader range of clay systems. In the future, we aim to use the PMFs in this study to develop a coarse-grained mesoscales of hydrated Cu-MMT, Ca-MMT and Na-MMT and examine their mechanical properties.

ACKNOWLEDGMENTS

This work is financially supported by the Nuclear Waste Management Organization, the Natural Science and Engineering Research Council (NSERC), and Mitacs. We also thank the Digital Research Alliance of Canada and Centre for Advanced Computing at Queen's University for generous allocation of computer resources.

-
- [1] S. Guggenheim, J. M. Adams, D. Bain, F. Bergaya, M. F. Brigatti, V. Drits, M. L. Formoso, E. Galán, T. Kogure, and H. Stanjek, Summary of recommendations of nomenclature committees relevant to clay mineralogy: report of the association internationale pour l'étude des argiles (aipea) nomenclature committee for 2006, *Clays and Clay minerals* **54**, 761 (2006).
 - [2] H. H. Murray, Bentonite applications, *Developments in Clay Science* **2**, 111 (2006).
 - [3] A. G. Clem and R. W. Doehler, Industrial applications of bentonite, *Clays and Clay minerals* **10**, 272 (1961).
 - [4] P. Abootalebi and G. Siemens, Thermal properties of engineered barriers for a canadian deep geological repository, *Canadian Geotechnical Journal* **55**, 759 (2018).
 - [5] F. Uddin, Clays, nanoclays, and montmorillonite minerals, *Metallurgical and Materials Transactions A* **39**, 2804 (2008).
 - [6] A. T. Bourgoynne, K. K. Millheim, M. E. Chenevert, F. S. Young, *et al.*, *Applied drilling engineering*, Vol. 2 (Society of Petroleum Engineers Richardson, 1986).
 - [7] M. G. Temraz and I. Hassani, Mineralogy and rheological properties of some egyptian bentonite for drilling fluids, *Journal of Natural Gas Science and Engineering* **31**, 791 (2016).
 - [8] R. O. Afolabi, O. D. Orodu, and V. E. Efeovbokhan, Properties and application of nigerian bentonite clay deposits for drilling mud formulation: recent advances and future prospects, *Applied Clay Science* **143**, 39 (2017).
 - [9] D. D. Carr, A. F. Alsobrook, and G. Austin, *Industrial minerals and rocks* (Society for mining metallurgy and exploration, 1994).
 - [10] J.-H. Park, H.-J. Shin, M. H. Kim, J.-S. Kim, N. Kang, J.-Y. Lee, K.-T. Kim, J. I. Lee, and D.-D. Kim, Application of montmorillonite in bentonite as a pharmaceutical excipient in drug delivery systems, *Journal of Pharmaceutical Investigation* **46**, 363 (2016).
 - [11] R. H. S. Robertson, Fullers earth: a history of calcium montmorillonite, (No Title) (1986).

- [12] E. Alvarez-Ayuso and A. García-Sánchez, Removal of heavy metals from waste waters by natural and na-exchanged bentonites, *Clays and Clay minerals* **51**, 475 (2003).
- [13] X. Liu, C. Tournassat, S. Grangeon, A. G. Kalinichev, Y. Takahashi, and M. Marques Fernandes, Molecular-level understanding of metal ion retention in clay-rich materials, *Nature Reviews Earth & Environment* **3**, 461 (2022).
- [14] P. Sellin and O. X. Leupin, The use of clay as an engineered barrier in radioactive-waste management—a review, *Clays and Clay Minerals* **61**, 477 (2013).
- [15] B. Grambow, Geological disposal of radioactive waste in clay, *Elements* **12**, 239 (2016).
- [16] N. Giroud, Y. Tomonaga, P. Wersin, S. Briggs, F. King, T. Vogt, and N. Diomidis, On the fate of oxygen in a spent fuel emplacement drift in opalinus clay, *Applied geochemistry* **97**, 270 (2018).
- [17] SKB, Post-closure safety for the final repository for spent nuclear fuel at forsmark. buffer, backfill and closure process report, psar version (2022).
- [18] J. Aromaa, M. Kekkonen, M. Mousapour, A. Jokilaakso, and M. Lundström, The oxidation of copper in air at temperatures up to 100 c, *Corrosion and Materials Degradation* **2**, 625 (2021).
- [19] D. Kong, C. Dong, A. Xu, C. Man, C. He, and X. Li, Effect of sulfide concentration on copper corrosion in anoxic chloride-containing solutions, *Journal of Materials Engineering and Performance* **26**, 1741 (2017).
- [20] F. Uddin *et al.*, *Montmorillonite: An introduction to properties and utilization*, Vol. 817 (IntechOpen London, UK, 2018).
- [21] J. R. Booker, R. Brachman, R. Quigley, and R. K. Rowe, *Barrier systems for waste disposal facilities* (Crc Press, 2004).
- [22] I. Odom, Smectite clay minerals: properties and uses, *Philosophical Transactions of the Royal Society of London. Series A, Mathematical and Physical Sciences* **311**, 391 (1984).
- [23] R. Anderson, I. Ratcliffe, H. Greenwell, P. Williams, S. Cliffe, and P. Coveney, Clay swelling—a challenge in the oilfield, *Earth-Science Reviews* **98**, 201 (2010).
- [24] R. T. Cygan, J. A. Greathouse, and A. G. Kalinichev, Advances in clayff molecular simulation of layered and nanoporous materials and their aqueous interfaces, *The Journal of Physical Chemistry C* **125**, 17573 (2021).
- [25] K. Norrish, Crystalline swelling of montmorillonite: manner of swelling of montmorillonite, *Nature* **173**, 256 (1954).
- [26] K. Norrish, The swelling of montmorillonite, *Discussions of the Faraday society* **18**, 120 (1954).
- [27] D. Fink and G. Thomas, X-ray studies of crystalline swelling in montmorillonites, *Soil Science Society of America Journal* **28**, 747 (1964).
- [28] Y. Zhang, J. Oestreicher, W. J. Binns, S. Briggs, C. S. Kim, and L. K. Béland, A coarse-grained interaction model for sodium dominant montmorillonite, *Langmuir* **38**, 13226 (2022).
- [29] D. Dixon, Review of the thmc properties of mx-80 bentonite, in *Nuclear Waste Management Organization, NWMO TR-2019-07, Toronto* (2019).
- [30] I. Ravina and P. F. Low, Change of b-dimension with swelling of montmorillonite, *Clays and Clay Minerals* **25**, 201 (1977).
- [31] L. Zhang, X. Lu, X. Liu, J. Zhou, and H. Zhou, Hydration and mobility of interlayer ions of (na x, ca y)-montmorillonite: a molecular dynamics study, *The Journal of Physical Chemistry C* **118**, 29811 (2014).
- [32] W. R. Foster, J. Savins, and J. Waite, Lattice expansion and rheological behavior relationships in water-montmorillonite systems, *Clays and Clay Minerals* **3**, 296 (1954).
- [33] A. Meleshyn and C. Bunnenberg, The gap between crystalline and osmotic swelling of na-montmorillonite: A monte carlo study, *The Journal of chemical physics* **122** (2005).
- [34] B. V. Derjaguin, Theory of the stability of strongly charged lyophobic sol and of the adhesion of strongly charged particles in solutions of electrolytes, *Acta phys. chim. URSS* **14**, 633 (1941).
- [35] R. M. Pashley and J. N. Israelachvili, Molecular layering of water in thin films between mica surfaces and its relation to hydration forces, *Journal of colloid and interface science* **101**, 511 (1984).
- [36] J. N. Israelachvili and R. M. Pashley, Molecular layering of water at surfaces and origin of repulsive hydration forces, *Nature* **306**, 249 (1983).
- [37] R. Jellander, S. Marčelja, and J. Quirk, Attractive double-layer interactions between calcium clay particles, *Journal of Colloid and Interface Science* **126**, 194 (1988).
- [38] J. Du, A. Zhou, X. Lin, Y. Bu, and J. Kodikara, Revealing expansion mechanism of cement-stabilized expansive soil with different interlayer cations through molecular dynamics simulations, *The Journal of Physical Chemistry C* **124**, 14672 (2020).
- [39] R. T. Cygan, J.-J. Liang, and A. G. Kalinichev, Molecular models of hydroxide, oxyhydroxide, and clay phases and the development of a general force field, *The Journal of Physical Chemistry B* **108**, 1255 (2004).
- [40] T. A. Ho, L. J. Criscenti, and J. A. Greathouse, Revealing transition states during the hydration of clay minerals, *The journal of physical chemistry letters* **10**, 3704 (2019).
- [41] T. Honorio, L. Brochard, and M. Vandamme, Hydration phase diagram of clay particles from molecular simulations, *Langmuir* **33**, 12766 (2017).
- [42] L. Sun, J. T. Hirvi, T. Schatz, S. Kasa, and T. A. Pakkanen, Estimation of montmorillonite swelling pressure: A molecular dynamics approach, *The Journal of Physical Chemistry C* **119**, 19863 (2015).
- [43] B. Akinwunmi, J. T. Hirvi, S. Kasa, and T. A. Pakkanen, Swelling pressure of na-and ca-montmorillonites in saline environments: A molecular dynamics study, *Chemical Physics* **528**, 110511 (2020).
- [44] B. Akinwunmi, *Molecular dynamics study of the bentonite barrier: effects of salinity and temperature on the swelling pressure*, Ph.D. thesis, Itä-Suomen yliopisto (2020).
- [45] P. Giannozzi, S. Baroni, N. Bonini, M. Calandra, R. Car, C. Cavazzoni, D. Ceresoli, G. L. Chiarotti, M. Cococcioni, I. Dabo, *et al.*, Quantum espresso: a modular and open-source software project for quantum simulations of materials, *Journal of physics: Condensed matter* **21**, 395502 (2009).
- [46] P. E. Blöchl, Projector augmented-wave method, *Physical review B* **50**, 17953 (1994).
- [47] A. Dal Corso, Pseudopotentials periodic table: From h

- to pu, *Computational Materials Science* **95**, 337 (2014).
- [48] We used the pseudopotentials mg.pbe-spn-kjpaw-psl.1.0.0.upf, al.pbe-nl-kjpaw-psl.1.0.0.upf, o.pbe-n-kjpaw-psl.1.0.0.upf, h.pbe-kjpaw-psl.1.0.0.upf, si.pbe-nl-kjpaw-psl.1.0.0.upf, cu.pbe-dn-kjpaw-psl.1.0.0.upf, and ca.pbe-spn-kjpaw-psl.1.0.0.upf from (<http://www.quantum-espresso.org>), .
- [49] J. P. Perdew, K. Burke, and M. Ernzerhof, Generalized gradient approximation made simple, *Physical review letters* **77**, 3865 (1996).
- [50] M. Holmboe, Atom: A matlab package for manipulation of molecular systems, *Clays and clay minerals* **67**, 419 (2019).
- [51] H. J. Monkhorst and J. D. Pack, Special points for brillouin-zone integrations, *Physical review B* **13**, 5188 (1976).
- [52] R. Fletcher, *Practical methods of optimization* (John Wiley & Sons, 2000).
- [53] D. Berthelot, Sur le mélange des gaz, *Compt. Rendus* **126**, 15 (1898).
- [54] H. J. Berendsen, J. P. Postma, W. F. van Gunsteren, and J. Hermans, Interaction models for water in relation to protein hydration, in *Intermolecular forces: proceedings of the fourteenth Jerusalem symposium on quantum chemistry and biochemistry held in jerusalem, israel, april 13-16, 1981* (Springer, 1981) pp. 331-342.
- [55] T. R. Underwood and I. C. Bourg, Large-scale molecular dynamics simulation of the dehydration of a suspension of smectite clay nanoparticles, *The Journal of Physical Chemistry C* **124**, 3702 (2020).
- [56] A. Dufresne, J. Arayro, T. Zhou, K. Ioannidou, F.-J. Ulm, R. Pellenq, and L. K. Béland, Atomistic and mesoscale simulation of sodium and potassium adsorption in cement paste, *The Journal of chemical physics* **149** (2018).
- [57] J. A. Greathouse, J. S. Durkin, J. P. Larentzos, and R. T. Cygan, Implementation of a morse potential to model hydroxyl behavior in phyllosilicates, *The Journal of chemical physics* **130** (2009).
- [58] M. Pouvreau, J. A. Greathouse, R. T. Cygan, and A. G. Kalinichev, Structure of hydrated kaolinite edge surfaces: Dft results and further development of the clayff classical force field with metal-o-h angle bending terms, *The Journal of Physical Chemistry C* **123**, 11628 (2019).
- [59] L. N. Lammers, I. C. Bourg, M. Okumura, K. Koluri, G. Sposito, and M. Machida, Molecular dynamics simulations of cesium adsorption on illite nanoparticles, *Journal of colloid and interface science* **490**, 608 (2017).
- [60] M. Pouvreau, J. A. Greathouse, R. T. Cygan, and A. G. Kalinichev, Structure of hydrated gibbsite and brucite edge surfaces: Dft results and further development of the clayff classical force field with metal-o-h angle bending terms, *The Journal of Physical Chemistry C* **121**, 14757 (2017).
- [61] S. Plimpton, Fast parallel algorithms for short-range molecular dynamics, *Journal of computational physics* **117**, 1 (1995).
- [62] A. P. Thompson, H. M. Aktulga, R. Berger, D. S. Bolintineanu, W. M. Brown, P. S. Crozier, P. J. in't Veld, A. Kohlmeyer, S. G. Moore, T. D. Nguyen, *et al.*, LAMMPS-a flexible simulation tool for particle-based materials modeling at the atomic, meso, and continuum scales, *Computer Physics Communications* **271**, 108171 (2022).
- [63] M. R. Hestenes, E. Stiefel, *et al.*, Methods of conjugate gradients for solving linear systems, *Journal of research of the National Bureau of Standards* **49**, 409 (1952).
- [64] S. Majidi, H. Erfan-Niya, J. Azamat, E. R. Cruz-Chú, and J. H. Walther, The performance of a c2n membrane for heavy metal ions removal from water under external electric field, *Separation and Purification Technology* **289**, 120770 (2022).
- [65] V. Moses, Ö. T. Bishop, and K. A. Lobb, The evaluation and validation of copper (ii) force field parameters of the auxiliary activity family 9 enzymes, *Chemical Physics Letters* **678**, 91 (2017).
- [66] K. Anitha, S. Namsani, and J. K. Singh, Removal of heavy metal ions using a functionalized single-walled carbon nanotube: a molecular dynamics study, *The Journal of Physical Chemistry A* **119**, 8349 (2015).
- [67] P. Li and K. M. Merz Jr, Taking into account the ion-induced dipole interaction in the nonbonded model of ions, *Journal of chemical theory and computation* **10**, 289 (2014).
- [68] P. Guan, D. McKenzie, and B. Pailthorpe, Md simulations of ag film growth using the lennard-jones potential, *Journal of Physics: Condensed Matter* **8**, 8753 (1996).
- [69] K. Louw, B. Bradshaw-Hajek, and J. Hill, Interaction of ferric ions with europium metal organic framework and application to mineral processing sensing, *Philosophical Magazine* **102**, 1231 (2022).
- [70] T. Akiner, H. Ertürk, and K. Atalık, Prediction of thermal conductivity and shear viscosity of water-cu nanofluids using equilibrium molecular dynamics, in *ASME International Mechanical Engineering Congress and Exposition*, Vol. 56369 (American Society of Mechanical Engineers, 2013) p. V08CT09A012.
- [71] H. Khanmohammadi, B. Bayati, J. Rahbar-Shahrrouzi, A.-A. Babaluo, and A. Ghorbani, Molecular simulation of the ion exchange behavior of cu²⁺, cd²⁺ and pb²⁺ ions on different zeolites exchanged with sodium, *Journal of Environmental Chemical Engineering* **7**, 103040 (2019).
- [72] J. Torras and C. Aleman, Determination of new cu⁺, cu²⁺, and zn²⁺ lennard-jones ion parameters in acetonitrile, *The Journal of Physical Chemistry B* **117**, 10513 (2013).
- [73] P. Li, B. P. Roberts, D. K. Chakravorty, and K. M. Merz Jr, Rational design of particle mesh ewald compatible lennard-jones parameters for+ 2 metal cations in explicit solvent, *Journal of chemical theory and computation* **9**, 2733 (2013).
- [74] Q. Liao, S. C. L. Kamerlin, and B. Strodel, Development and application of a nonbonded cu²⁺ model that includes the jahn-teller effect, *The Journal of Physical Chemistry Letters* **6**, 2657 (2015).
- [75] E. Duffour and P. Malfreyt, Md simulations of the collision between a copper ion and a polyethylene surface: an application to the plasma-insulating material interaction, *Polymer* **45**, 4565 (2004).
- [76] C. Zhang, L. Liu, and H. Jia, Molecular dynamics study of the exchange processes of heavy metals into montmorillonite: Characterization of hydrated edge surfaces and dynamic exchange mechanism, *Applied Geochemistry* **150**, 105587 (2023).
- [77] A. W. Knight, P. Ilani-Kashkouli, J. A. Harvey, J. A. Greathouse, T. A. Ho, N. Kabengi, and A. G. Ilgen, In-

- terfacial reactions of cu (ii) adsorption and hydrolysis driven by nano-scale confinement, *Environmental Science: Nano* **7**, 68 (2020).
- [78] S. Izvekov and G. A. Voth, Car-parrinello molecular dynamics simulation of liquid water: New results, *The Journal of chemical physics* **116**, 10372 (2002).
- [79] D. Trzesniak, A.-P. E. Kunz, and W. F. van Gunsteren, A comparison of methods to compute the potential of mean force, *ChemPhysChem* **8**, 162 (2007).
- [80] J. Kästner, Umbrella sampling, *Wiley Interdisciplinary Reviews: Computational Molecular Science* **1**, 932 (2011).
- [81] M. Sprik and G. Ciccotti, Free energy from constrained molecular dynamics, *The Journal of chemical physics* **109**, 7737 (1998).
- [82] V. K. Voora, W. Al-Saidi, and K. D. Jordan, Density functional theory study of pyrophyllite and montmorillonites (m= li, na, k, mg, and ca): Role of dispersion interactions, *The Journal of Physical Chemistry A* **115**, 9695 (2011).
- [83] G. W. Marini, K. R. Liedl, and B. M. Rode, Investigation of cu²⁺ hydration and the jahn-teller effect in solution by qm/mm monte carlo simulations, *The Journal of Physical Chemistry A* **103**, 11387 (1999).
- [84] D. T. Bowron, M. Amboage, R. Boada, A. Freeman, S. Hayama, and S. Díaz-Moreno, The hydration structure of cu²⁺: more tetrahedral than octahedral?, *RSC Advances* **3**, 17803 (2013).
- [85] C. F. Schwenk and B. M. Rode, Extended ab initio quantum mechanical/molecular mechanical molecular dynamics simulations of hydrated cu²⁺, *The Journal of chemical physics* **119**, 9523 (2003).
- [86] A. C. Van Duin, V. S. Bryantsev, M. S. Diallo, W. A. Goddard, O. Rahaman, D. J. Doren, D. Raymand, and K. Hermansson, Development and validation of a reaxff reactive force field for cu cation/water interactions and copper metal/metal oxide/metal hydroxide condensed phases, *The Journal of Physical Chemistry A* **114**, 9507 (2010).
- [87] H. Ohtaki and T. Radnai, Structure and dynamics of hydrated ions, *Chemical reviews* **93**, 1157 (1993).
- [88] S. Amira, D. Spångberg, and K. Hermansson, Distorted five-fold coordination of cu²⁺(aq) from a car-parrinello molecular dynamics simulation, *Physical Chemistry Chemical Physics* **7**, 2874 (2005).
- [89] M. Magini, Coordination of copper (ii). evidence of the jahn-teller effect in aqueous perchlorate solutions, *Inorganic Chemistry* **21**, 1535 (1982).
- [90] A. Musinu, G. Paschina, G. Piccaluga, and M. Magini, Coordination of copper (ii) in aqueous copper sulfate solution, *Inorganic Chemistry* **22**, 1184 (1983).
- [91] A. Pasquarello, I. Petri, P. S. Salmon, O. Parisel, R. Car, É. Tóth, D. H. Powell, H. E. Fischer, L. Helm, and A. E. Merbach, First solvation shell of the cu (ii) aqua ion: evidence for fivefold coordination, *Science* **291**, 856 (2001).
- [92] B. Beagley, A. Eriksson, J. Lindgren, I. Persson, L. Pettersson, M. Sandstrom, U. Wahlgren, and E. White, A computational and experimental study on the jahn-teller effect in the hydrated copper (ii) ion. comparisons with hydrated nickel (ii) ions in aqueous solution and solid tutton's salts, *Journal of Physics: Condensed Matter* **1**, 2395 (1989).
- [93] G. Clark, R. Grim, and W. Bradley, A study of the behavior of montmorillonite upon wetting, *Zeitschrift für Kristallographie-Crystalline Materials* **97**, 216 (1937).
- [94] M. Antognozzi, A. Humphris, and M. Miles, Observation of molecular layering in a confined water film and study of the layers viscoelastic properties, *Applied Physics Letters* **78**, 300 (2001).
- [95] B. Akinwunmi, L. Sun, J. T. Hirvi, S. Kasa, and T. A. Pakkanen, Influence of temperature on the swelling pressure of bentonite clay, *Chemical Physics* **516**, 177 (2019).
- [96] S. S. Agus and T. Schanz, A method for predicting swelling pressure of compacted bentonites, *Acta Geotechnica* **3**, 125 (2008).
- [97] S. Kumpulainen and L. Kiviranta, *Mineralogical, chemical and physical study of potential buffer and backfill materials from ABM. Test Package 1*, Tech. Rep. (Posiva Oy, 2011).
- [98] O. Karnland, S. Olsson, and U. Nilsson, *Mineralogy and sealing properties of various bentonites and smectite-rich clay materials*, Tech. Rep. (Swedish Nuclear Fuel and Waste Management Co., 2006).
- [99] F. Bucher and U. Spiegel, *Quelldruck von hochverdichteten Bentoniten* (Nagra, 1984).
- [100] P. Sitz *et al.*, Materialuntersuchungen für mehrkomponentensysteme auf ton/bentonit basis für dichtung und lastabtrag (1997).
- [101] F. Jalilehvand, D. Spångberg, P. Lindqvist-Reis, K. Hermansson, I. Persson, and M. Sandström, Hydration of the calcium ion. an exafs, large-angle x-ray scattering, and molecular dynamics simulation study, *Journal of the American Chemical Society* **123**, 431 (2001).
- [102] J. L. Fulton, S. M. Heald, Y. S. Badyal, and J. Simonson, Understanding the effects of concentration on the solvation structure of ca²⁺ in aqueous solution. i: The perspective on local structure from exafs and xanes, *The Journal of Physical Chemistry A* **107**, 4688 (2003).
- [103] P. D'Angelo, P.-E. Petit, and N. V. Pavel, Double-electron excitation channels at the ca²⁺ k-edge of hydrated calcium ion, *The Journal of Physical Chemistry B* **108**, 11857 (2004).
- [104] S. Ansell, A. Barnes, P. Mason, G. Neilson, and S. Ramos, X-ray and neutron scattering studies of the hydration structure of alkali ions in concentrated aqueous solutions, *Biophysical chemistry* **124**, 171 (2006).
- [105] M. Holmboe and I. C. Bourg, Molecular dynamics simulations of water and sodium diffusion in smectite interlayer nanopores as a function of pore size and temperature, *The Journal of Physical Chemistry C* **118**, 1001 (2014).
- [106] J. A. Greathouse, R. T. Cygan, J. T. Fredrich, and G. R. Jerauld, Molecular dynamics simulation of diffusion and electrical conductivity in montmorillonite interlayers, *The Journal of Physical Chemistry C* **120**, 1640 (2016).
- [107] Y. Li, X. Wang, and J. Wang, Cation exchange, interlayer spacing, and thermal analysis of na/ca-montmorillonite modified with alkaline and alkaline earth metal ions, *Journal of thermal analysis and calorimetry* **110**, 1199 (2012).
- [108] H. A. Lorentz, Ueber die anwendung des satzes vom virial in der kinetischen theorie der gase, *Annalen der physik* **248**, 127 (1881).
- [109] J. H. Lee and S. Guggenheim, Single crystal x-ray refine-

- ment of pyrophyllite-1 tc, *American Mineralogist* **66**, 350 (1981).
- [110] B. Akinwunmi, F. E. Kporha, J. T. Hirvi, S. Kasa, and T. A. Pakkanen, Atomistic simulations of the swelling behaviour of na-montmorillonite in mixed nacl and cacl₂ solutions, *Chemical Physics* **533**, 110712 (2020).
 - [111] Z. Zeng, Y.-J. Cui, and J. Talandier, Evaluation of swelling pressure of bentonite/claystone mixtures from pore size distribution, *Acta Geotechnica* **18**, 1671 (2023).
 - [112] N. Saiyouri, D. Tessier, and P.-Y. Hicher, Experimental study of swelling in unsaturated compacted clays, *Clay minerals* **39**, 469 (2004).
 - [113] N. Saiyouri, P. Hicher, and D. Tessier, Microstructural approach and transfer water modelling in highly compacted unsaturated swelling clays, *Mechanics of Cohesive-frictional Materials: An International Journal on Experiments, Modelling and Computation of Materials and Structures* **5**, 41 (2000).